Hindawi
Advances in Materials Science and Engineering
Volume 2021, Article ID 1518763, 12 pages
https://doi.org/10.1155/2021/1518763

Research Article

Numerical Analysis of the Seismic Response of Tunnel Composite Lining Structures across an Active Fault

Zude Ding, Mingrong Liao, Nanrun Xiao, and Xiaoqin Li

Faculty of Civil Engineering and Mechanics, Kunming University of Science and Technology, Kunming 650500, China

Correspondence should be addressed to Zude Ding; dzdvsdt@163.com

Received 14 August 2021; Accepted 19 November 2021; Published 3 December 2021

Academic Editor: José António Fonseca de Oliveira Correia

The mechanical properties of high-toughness engineering cementitious composites (ECC) were tested, and a damage constitutive model of the materials was constructed. A new aseismic composite structure was then built on the basis of this model by combining aseismic joints, damping layers, traditional reinforced concrete linings, and ECC linings. A series of 3D dynamic-response numerical models considering the composite structure-surrounding rock-fault interaction were established to explore the seismic response characteristics and aseismic performance of the composite structures. The adaptability of the structures to the seismic intensity and direction was also discussed. Results showed that the ECC material displays excellent tensile and compressive toughness, with respective peak tensile and compressive strains of approximately 300- and 3-fold greater than those of ordinary concrete at the same strength grade. The seismic response law of the new composite lining structure was similar to that of the conventional composite structure. The lining in the fault zone and adjacent area showed obvious acceleration amplification responses, and the stress and displacement responses were fairly large. The lining in the fault zone was the weak part of the composite structures. Compared with the conventional aseismic composite structure, the new composite lining structure effectively reduced the acceleration amplification and displacement responses in the fault area. The damage degree of the new composite structure was notably reduced and the damage area was smaller compared with those of the conventional composite structure; these findings demonstrate that the former shows better aseismic effects than the latter. The intensity and direction of seismic waves influenced the damage of the composite structures to some extent, and the applicability of the new composite structure to lateral seismic waves is significantly better than that to axial waves. More importantly, under the action of different seismic intensities and directions, the damage degree and distribution area of the new composite structure were significantly smaller than those of the conventional composite lining structure.

1. Introduction

Earthquake damage investigations have found serious damage in tunnels running across a fault following a strong seismic event [1–3]. Therefore, research on the seismic response and aseismic performance of tunnels across faults has attracted widespread attention. For example, Li and He et al. [4, 5] combined models and numerical analysis to study the seismic response properties and damage mechanism of tunnels crossing fault fracture zones; the authors revealed that the linings of fault fracture zones and adjacent areas are highly prone to damage. Liu et al. [6] carried out a model test of the seismic response of a cross-fault tunnel, and results showed intense forces at the arch springing of the lining under the action of seismic waves. The authors thus recommended strengthening the aseismic fortification of the structure. Geng et al. [7] analyzed the seismic effect of a damping layer in an aseismic cross-fault tunnel and showed that the damping layer can reduce the damage of the lining under a seismic load and improve its aseismic performance. Wang et al. [8] studied the seismic effect of different aseismic joints, analyzed the relationship between these joints and the aseismic effect, and then obtained the optimal distance of aseismic joints. Jin [9] proposed an aseismic structure combining aseismic joints and a damping layer and then studied the aseismic effect of the resulting composite structure.

The studies described above mainly focus on the seismic damage mechanism of cross-fault tunnels, as well as aseismic

measures, such as damping layers, aseismic joints, and segmental joints; however, they rarely combine high-performance materials with an exploration of approaches to improve the lining. Engineering cementitious composites (ECC) refer to fiber-reinforced cementitious composite materials characterized with good deformation ability, strain hardening ability, and crack control [10]. Owing to the inhibitory effect of the fibers of ECC on the appearance and development of early shrinkage cracks, the composites show excellent durability [11, 12]. ECC have excellent tensile and compressive toughness and energy dissipation capacity, as well as strong adaptability to complex stress conditions under seismic events; thus, these materials have been used in the aseismic field of high-rise building and bridge [13]. However, no relevant research report on the application of ECC materials in the aseismic of tunnel structures has yet been published. Hence, in this work, reinforced ECC (R/ECC) is used to replace traditional reinforced concrete (RC) linings partially to construct a composite lining structure based on the mechanical properties of the ECC materials. Numerical analysis is then used to establish a 3D seismic-response calculation model of the tunnel composite lining structure system-surrounding rock-fault interaction, and the seismic response properties, aseismic performance, and applicability of the composite structure are discussed.

2. ECC Material Mechanical Performance Test

The relevant standards of concrete mechanical performance testing are employed to conduct uniaxial tensile and compression experiments of the ECC materials [14]. A thin plate specimen with a thickness of 15 mm and length of 330 mm is used for the tensile tests. The test section length is 50 mm. The test piece is fixed on an electronic universal testing machine with a loading fixture. The loading process is controlled by displacement, and the loading rate is set to 0.15 mm/min. The tensile strain is measured by installing an extensometer with a measuring range of 5 mm and an accuracy of 0.025 mm in the test section of the specimen. The compression test uses a cube specimen with a side length of 100 mm, and the specimen is loaded into a hydraulic servo universal testing machine. Images of the tensile and compression tests are shown in Figure 1, and the stress-strain relationship of the specimens is shown in Figure 2.

Figure 2(a) shows that the ECC tensile stress-strain curves can be divided into three stages, namely, elasticity, strain hardening, and strain softening. The peak tensile stresses of the three ECC specimens are approximately 3.71, 3.67, and 3.64 MPa, respectively, and the corresponding peak tensile strains are approximately 2.93%, 3.33%, and 3.54%, respectively. The average peak tensile stress and tensile strain are 3.67 MPa and 3.27%, respectively. Interestingly, the peak tensile strain of the ECC is over 300 times greater than that of ordinary concrete. Thus, the ECC has better tensile strain hardening properties and tensile toughness than ordinary concrete and can effectively make up for the shortcomings of the latter, which include poor toughness and easy cracking.

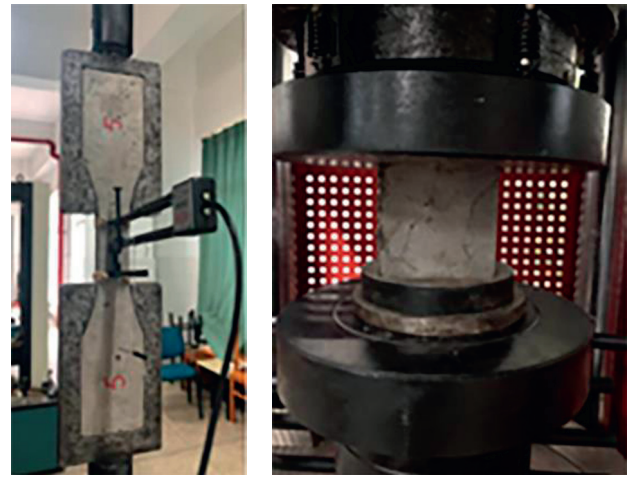

(a) (b)

Figure 1: Tensile and compression test. (a) Tensile test. (b) Compression test.

The results of the ECC uniaxial compression test reveal that the ECC compressive stress-strain curve presents nonlinear properties. Among the three specimens, the average peak stress is 42.0 MPa, and the compressive strain corresponding to the peak stresses is 0.45%. The respective peak stress and strain of the ECC are approximately 1.4 and 3.0 times those of C30 concrete. Thus, the ECC has higher compressive strength and better compressive toughness than C30 concrete.

3. Material Model and Parameters

3.1. ECC and Concrete Model. The concrete damaged plasticity (CDP) model [15, 16] is selected to analyze the aseismic performance and describe the mechanical behavior of the ECC materials. The CDP model assumes that the failure modes of materials are mainly tensile cracking and compression crushing. The stress-cracking strain relationship under uniaxial tension and the stress-inelastic strain relationship under uniaxial compression are defined to describe the strain-softening properties of concrete tensile cracking and compression crushing. The ECC compressive stress-strain relationship can be determined by combining these properties of the ECC and expressed as follows [17]:

$$\sigma_c = \begin{cases} E_{c0}\varepsilon_c & 0 < \varepsilon_c < \varepsilon_{c0.4} \\ E_{c0}\varepsilon_c\left(1 - 0.39\dfrac{\varepsilon E_{c0}}{\sigma_{cp}} + 0.25\right) & \varepsilon_{c0.4} < \varepsilon_c < \varepsilon_{cp} \\ -9470.6\left(\varepsilon_c - \varepsilon_{cp}\right) + \sigma_{cp} & \varepsilon_{cp} < \varepsilon_c < \varepsilon_{cl} \\ -375.4\left(\varepsilon_c - \varepsilon_{cl}\right) + \sigma_{cl} & \varepsilon_{cl} < \varepsilon_c < \varepsilon_{cu} \end{cases}, \quad (1)$$

where E_{c0} is the initial Young's modulus of the ECC, $\varepsilon_{c0.4}$ is the corresponding strain value when the ECC stress reaches 40% of the ultimate strength, σ_{cp} and ε_{cp} are the respective peak uniaxial compressive stress value of the ECC and the

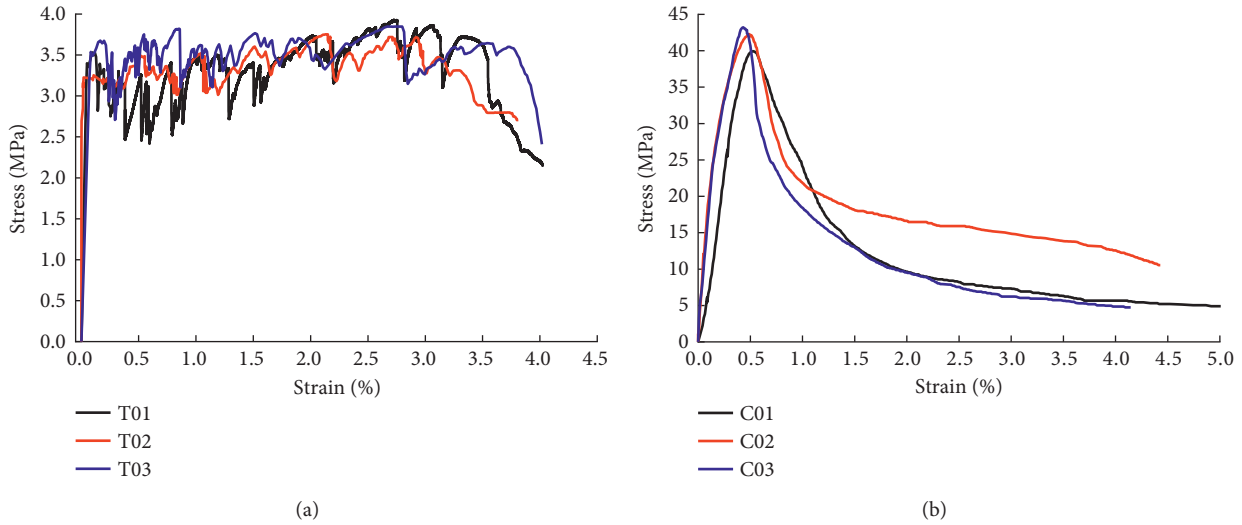

Figure 2: ECC uniaxial tensile and compression stress-strain curves. (a) Uniaxial tensile. (b) Uniaxial compression.

corresponding peak compressive stress-strain value, σ_{cl} and ε_{cl} are the respective stress and strain values at the turning point of the ECC compressive stress-strain curve, and σ_{cu} and ε_{cu} are the respective ECC uniaxial compressive ultimate stress and strain values corresponding to the ultimate stress.

The ECC tensile stress-strain relationship can be expressed as follows [18]:

$$\sigma_t = \begin{cases} \dfrac{\sigma_{t0}}{\varepsilon_{t0}}\varepsilon_t & 0 \le \varepsilon_t < \varepsilon_{t0} \\ \dfrac{\sigma_{tp} - \sigma_{t0}}{\varepsilon_{tp} - \varepsilon_{t0}}(\varepsilon - \varepsilon t0) + \sigma_{t0} & \varepsilon_{t0} \le \varepsilon_t < \varepsilon_{tp} \\ \dfrac{\sigma_{tp}(\varepsilon_{tu} - \varepsilon_t)}{\varepsilon_{tu} - \varepsilon_{tp}} & \varepsilon_{tp} \le \varepsilon_t < \varepsilon_{tu} \\ 0 & \varepsilon_{tu} \le \varepsilon_t \end{cases}, \quad (2)$$

where σ_{t0} and ε_{t0} are the ECC uniaxial tensile yield stress and yield strain, respectively, σ_{tp} and ε_{tp} are the ECC uniaxial tensile peak stress and strain corresponding to the peak stress, respectively, and σ_{tu} and ε_{tu} are the ECC uniaxial tensile limit stress and its ultimate strain corresponding to the limit stress, respectively.

The damage factor in the plastic damage model is determined according to Sidoroff's energy equivalence principle and written as follows [19]:

$$d_k = 1 - \left(\frac{\sigma_k}{E_0 \varepsilon_k}\right)^{0.5}, \quad (3)$$

where $k = c$ refers to compression, $k = t$ refers to tension, d_k is the damage variable, E_0 is the initial Young's modulus of the ECC, σ_k is the ECC stress, and ε_k is the ECC strain. The numerical simulation in this paper adopts monotonic loading, and the weight factor of stiffness recovery is taken as $w_c = 1$ and $w_t = 0$.

The ECC stress-strain curve is determined according to the existing tests [18, 20–28] in combination with the results of the mechanical properties of ECC materials that we have tested [29–31] and (1) and (2), as shown in the dotted line in Figure 3. In the calculations, the Young's modulus of ECC is 15 GPa, the Poisson's ratio is 0.2, and the unit weight is 19 kN/m^3. The mechanical parameters of the ECC damage model are shown in Table 1.

Ordinary tunnel linings commonly adopt C30 RC linings; the constitutive model of the concrete materials also adopts the CDP model to enable comparison with the ECC. The mechanical parameters for C30 concrete are determined according to concrete structural design standards [32] (Table 1). The concrete Young's modulus is 30 GPa, the Poisson's ratio is 0.2, and the unit weight is 25 kN/m^3. The relevant stress-strain curve is illustrated by the solid line in Figure 3.

3.2. Rebar and Surrounding Rock Model. The mechanical behavior of the lining rebars is simulated by a three-stage elastoplastic model [33], and the physical and mechanical parameters of these rebars are shown in Table 2. In the calculation model, the rebar reinforcement is embedded in the region of the concrete solid element, and the bond slip between rebars and concrete does not being considered in this paper.

The constitutive model of the surrounding rock adopts the Mohr–Coulomb (M–C) elastoplastic model. The physical and mechanical parameters of the hanging wall, footwall, and fault zone are determined by combining this model with the surrounding rock conditions of the project, and the results are shown in Table 3.

4. Tunnel Seismic Response Calculation Model

4.1. Establishment of the Seismic Response Model. The aseismic joints, damping layers, and their combined are often used in the aseismic design of tunnels. The existing

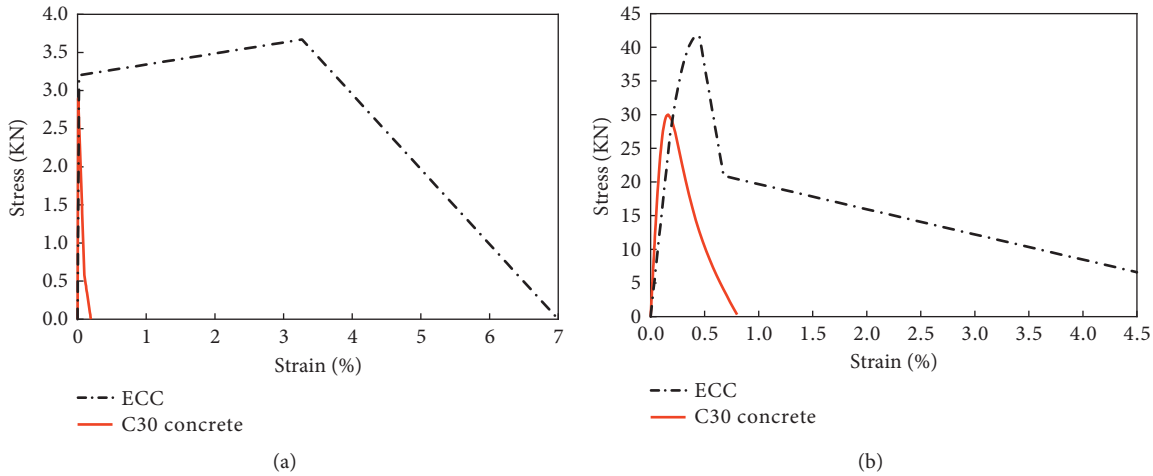

Figure 3: Constitutive model curves of the ECC and concrete materials. (a) Tensile stress-strain curves. (b) Compression stress-strain curves.

Table 1: Physical and mechanical parameters of the ECC and concrete materials.

Material	Experiment method	Yield stress (MPa)	Yield strain (%)	Peak stress (MPa)	Peak strain (%)	Ultimate stress (MPa)	Ultimate strain (%)	Young's Modulus (GPa)	Poisson's ratio	Density (kg/m^3)
C30 concrete	Uniaxial tensile	1.54	0.0051	2.89	0.01	0.18	0.19	30	0.2	2500
	Uniaxial compression	12	0.04	30.0	0.15	2.0	2.0			
ECC	Uniaxial tensile	3.2	0.021	3.67	3.27	--	7.0	15	0.2	1900
	Uniaxial compression	32.2	0.18	41.8	0.45	--	4.5			

Table 2: Physical and mechanical parameters of the rebars.

Young's Modulus(GPa)	Poisson's ratio	Yield strength (MPa)	Yield strain (%)	Ultimate strength (MPa)	Ultimate strain (%)
200	0.3	400	0.2	540	7.5

Table 3: Physical and mechanical parameters of the surrounding rock and fault fracture zone.

Material	Young's Modulus (GPa)	Density (kg/m^3)	Poisson's ratio	Cohesion (MPa)	Friction angle (°)
Rock	1.3	2000	0.39	0.12	22
Fault	0.5	2000	0.42	0.02	20

research shows that the optimal distance of the aseismic joints is 12 m [34, 35]. The damping layer is made of rubber material, the preferred thickness of the damping layer is 10 cm, and Young's modulus is 100 MPa [36, 37]. High-performance ECC materials are introduced to the conventional aseismic composite structure described above to improve the aseismic performance of the lining. Specifically, R/ECC linings are used to replace traditional RC linings partially and construct a new composite lining structure; the typical structure of this new composite lining is shown in Figure 4.

A seismic response calculation model was established by referring to a highway tunnel passing through the fault of the Xiaojiang active fault zone to explore the seismic response properties and aseismic performance of the novel composite lining structure. The tunnel is 2088 m long, and its maximum buried depth is approximately 269.56 m. The primary support of the tunnel consists of a steel mesh, I20a I–steel arches, and C25 shotcrete, with a thickness of 27 cm; the secondary lining is composed of C30 RC with a thickness of 60 cm. The dip angle of the reverse fault crossed by the tunnel is 50°–70°. According to the *Seismic Parameter Zonation Map of China*, the tunnel is located in a high seismic intensity area (8° under Chinese standards), where the peak acceleration is 0.2 g and the characteristic period is 0.45 s. In the seismic design of the tunnel, the seismic fortification intensity increased by one degree, and the peak acceleration of the tunnel is taken as 0.4 g (9° under Chinese standards).

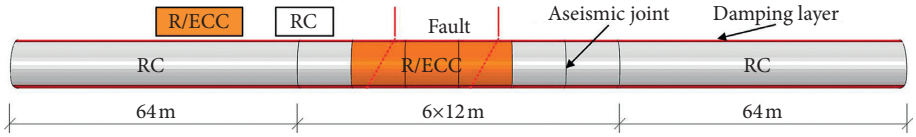

Figure 4: Composite lining structure.

According to the engineering geological and fault characteristics of the tunnel project, the buried depth of the tunnel is 50 m, the fault inclination is 60°, and the fault zone width is 20 m. Thus, the 3D seismic response calculation model could be established as shown in Figure 5. A 200 m long and 100 m width, and 100 m height model was built in the numerical analysis. Three lining sections (length, 72 m) are set as seismic fortification sections at the front and rear relative to the axial central section of the calculation model, and aseismic joints are set between each lining segment at intervals of 12 m. The damping layer is adopted by soft rubber, the thickness of the rubber is 10 cm, and Young's modulus is 100 MPa (Figure 4).

The model does not consider the role of the primary support, which is regarded as a reinforcement for the excavation disturbance of the surrounding rock. The damage model is used to describe the seismic damage behavior of the secondary lining, and the surrounding rock is simulated by the M–C elastoplastic model; both the lining and surrounding rock are simulated by three-dimensional eight-node (C3D8) reduced integral solid elements. Mesh division follows the principle that the size of the mesh elements is not greater than 1/8–1/10 of the seismic wavelength, and the mesh division of the lining and fault fracture zone should be appropriately intensified. The rebars adopt implanted truss elements, which are embedded in solid concrete elements. The interaction between the hanging wall, footwall, and fault fracture zone is simulated by the contact surface model. The normal contact behavior is calculated by the hard contact algorithm, the tangential contact behavior is described by setting the Coulomb contact model, and the tangential contact friction coefficient is taken as 0.3 [38, 39]. The interaction between adjacent lining segments is also simulated by the Coulomb contact model, and the tangential friction coefficient is 0.2. The mechanical behavior of the rubber damping layer is described by a linear elastic model. The dynamic artificial boundary adopts the infinite element boundary [40, 41] and uses Rayleigh damping to describe the damping properties of the surrounding rock-tunnel structure system. The damping ratio is 5%.

This paper selects typical Kobe seismic waves as an example for analysis to facilitate the calculations and determined the corresponding seismic response properties based on the type of engineering site and discusses the laws and applicability of seismic responses under different aseismic measures. The acceleration time history curve is obtained by using amplitude modulation, as shown in Figure 6. The equivalent nodal force of each node on the boundary is calculated on the basis of the Kobe seismic wave acceleration-time history data, and the seismic input is realized by applying the equivalent nodal force on the interface between the finite and infinite elements. Considering that the equivalent nodal force is applied one by one on the basis of the boundary nodes and that the corresponding equivalent nodal force-time history must be calculated at each node, this part of the workload is especially heavy for the 3D dynamic response calculation model. Thus, this paper compiles an infinite element boundary seismic input program based on the Python language and realizes the automatic input of the equivalent nodal force-time history.

4.2. Calculation Plan. In this work, two structural types are considered: the new composite lining structure (abbreviated as NCS) and a conventional composite lining structure (abbreviated as CCS). The new composite structure combines a damping layer, aseismic joints, RC lining, and R/ECC lining, and the R/ECC lining is arranged on the fault area (Figure 4). The conventional composite structure is composed of a damping layer, aseismic joints, and RC lining. The specific calculation plan is shown in Table 4. The three-dimensional seismic response calculation process of a cross-fault tunnel is divided into three steps. First, the pressure balance is calculated, after which the tunnel excavation and support are simulated; finally, the seismic response is simulated.

5. Seismic Response and Applicability Analyses of the Composite Structure

5.1. Seismic Response Analysis. During the seismic process, there was concentration stress of the lining in the area of the fault fracture zone. Therefore, this section analyzes the seismic response of the composite structure in this area from the four aspects of acceleration, stress, damage, and displacement response of the lining.

5.1.1. Acceleration Response. The peak acceleration data of the typical parts of the composite lining structure along the tunnel are extracted. The distribution curve of the peak acceleration of each typical part along the tunnel is shown in Figure 7. Here, the lining of the fault fracture zone shows an obvious acceleration amplification response. The closer the lining approaches the fault, the greater the peak acceleration of each typical part of the lining; conversely, the farther the lining is from the fault, the smaller the acceleration response. This finding shows that the lining of the fault fracture zone and adjacent area is fairly susceptible to seismic damage and must be fortified, consistent with the existing research conclusions. Compared with conventional aseismic structures, the new

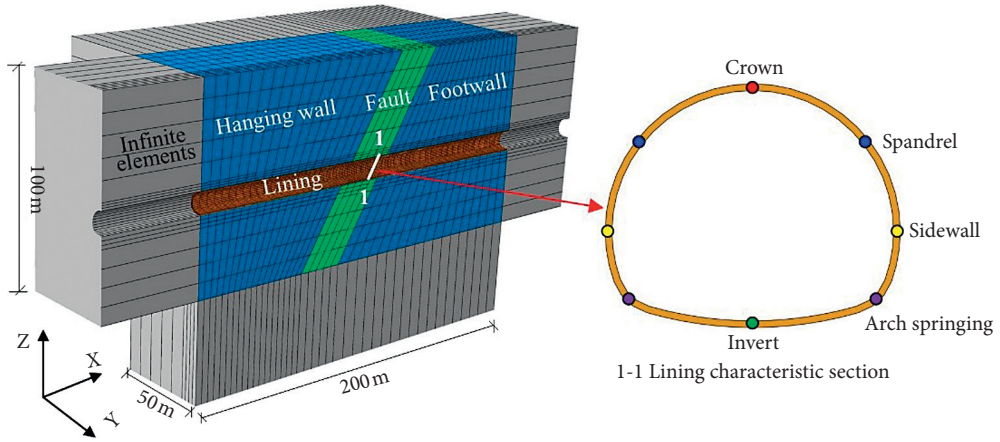

Figure 5: 3D seismic response calculation model of the tunnel crossing a fault.

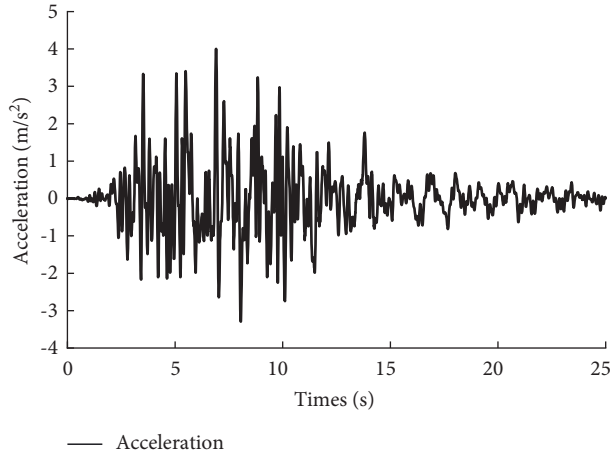

Figure 6: Seismic acceleration-time history curve.

Table 4: Calculation plan.

Calculation plan	Lining structure type	Seismic wave	Peak acceleration	Seismic direction
1–6	New composite structure (NCS), conventional composite structure (CCS)	Kobe wave	0.4 g, 0.6 g	Laterally, axial

composite lining structure system can effectively reduce the acceleration amplification response.

5.1.2. Stress Response. The lining section at the intersection of the footwall of the new composite structure and the fault fracture zone is selected for analysis, and the principal stress-time history curves of the lining crown, arch springing, and invert of the section are extracted, as shown in Figure 8. The principal stress-time history curves of each typical part of the lining are similar. The curves can be divided into three stages. The principal stress of the lining remains basically constant in the initial stage of seismic loading. Then (about 3 s), the principal stress of the lining begins to oscillate and increases rapidly. Finally, the stress fluctuation decreases and tends to stabilize, and it appears as a residual stress after the earthquake. Compared with those at the crown and invert, the residual stress at the arch springing is larger.

The distribution curve of the principal stress along the longitudinal direction of the tunnel at the arch springing of the composite structure is further extracted, as shown in Figure 9. The maximum and minimum principal stress at the arch springing of the lining is similarly distributed along the longitudinal direction of the tunnel, and both features show a significant increase in the fault area and adjacent fracture zone. The maximum principal stress appears at the arch springing of the lining in the fault area. By comparison, the principal stress of the new composite structure is smaller than that of the conventional composite structure in the fault fracture zone. Specifically, the maximum principal stress of the new composite structure is 0.5 MPa lower than that of the conventional composite structure, and the minimum principal stress is reduced by 2 MPa. It showed that the conventional structure is more vulnerable than the new structure.

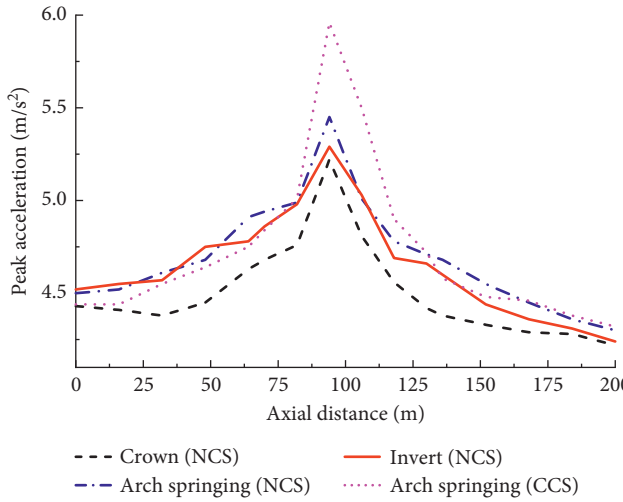

Figure 7: Changes in the peak acceleration of the composite structure along the length of the tunnel.

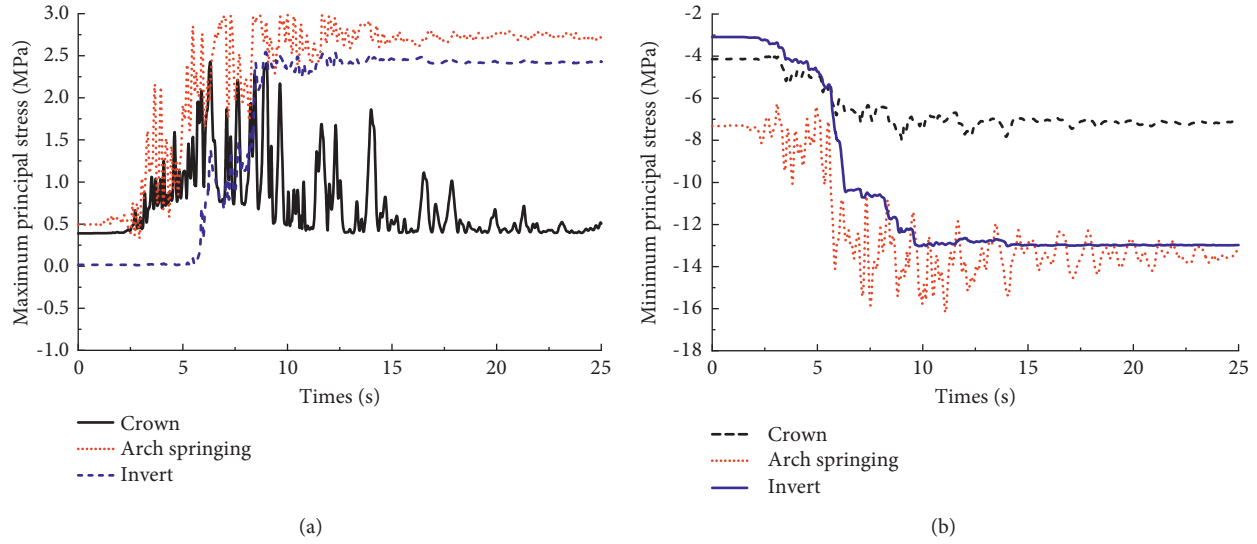

Figure 8: Principal stress-time history curve of typical parts of the lining. (a) Maximum principal stress. (b) Minimum principal stress.

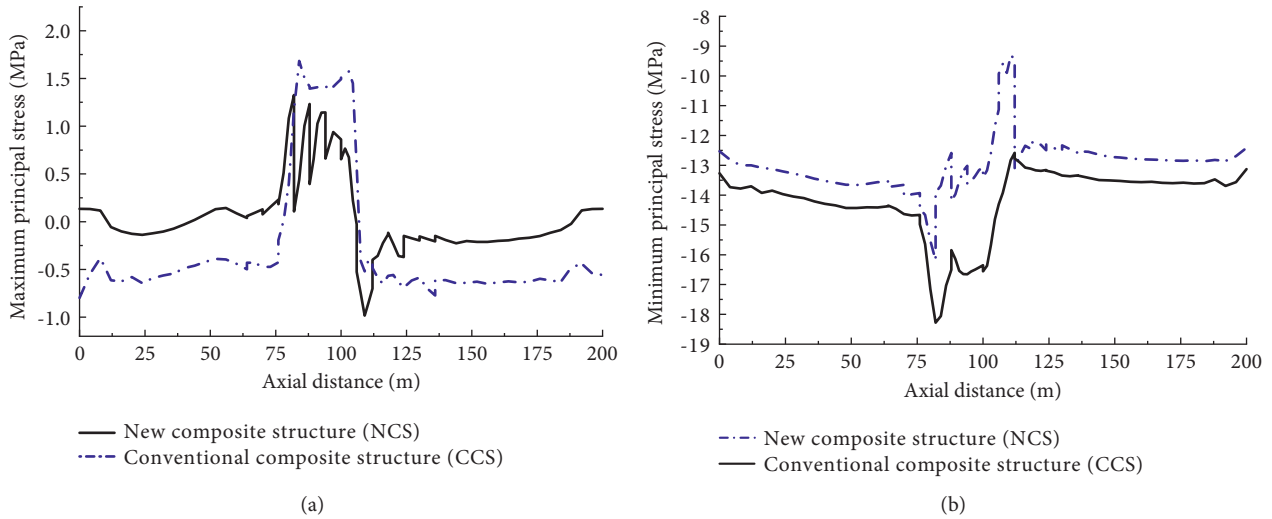

Figure 9: Distribution curve of the principal stress of the lining arch springing along the axial of the tunnel. (a) Maximum principal stress. (b) Minimum principal stress.

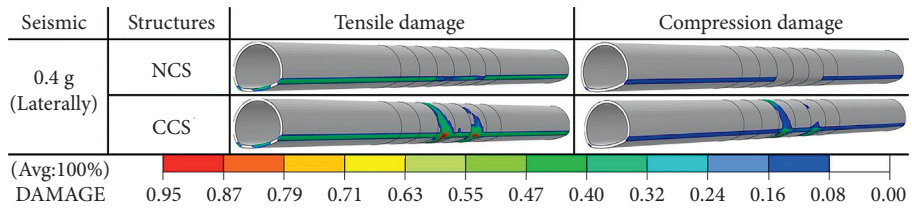

Figure 10: Lining damage distribution.

5.1.3. Damage Response. After the earthquake, the tensile and compressive damage distributions of the two composite lining structures are determined as shown in Figure 10. Here, the tensile damage values of the two composite structures are significantly greater than the corresponding compressive damage values; thus, the damage mechanism of the lining structures is mainly tensile damage. Compared with those of the conventional composite structure, the damage degree and damage area of the new composite structure are significantly reduced; thus, the latter has better aseismic effects than the former.

The time history curve of the tensile damage of typical parts of the lining and the distribution curve of tensile damage along the longitudinal direction of the tunnel are shown in Figures 11 and 12, respectively. Figure 11 shows that the seismic damage process of different typical parts of the lining is similar, which can be divided into three stages. In the initial stage of the seismic loading, the lining is basically undamaged; during the period of 6–15 s, the damage of the lining increases rapidly and then eventually stabilizes. After the earthquake, the tensile and compressive damage peak values of a typical cross section of the new composite lining structure are 0.18 and 0.03, respectively. By comparison, the tensile and compression damage peak values of the same cross section of the conventional composite structure lining are 0.87 and 0.24, respectively (Figure 10). Moreover, under the same seismic intensity, the respective maximum tensile and compressive damage values of the new composite structure are only 20.7% and 13.5% those of the former.

Analysis of Figure 12 reveals that replacement of the conventional composite structure with the new composite structure greatly reduces the damage of the structure in the fault and improves or even eliminates the damage concentration area of the former. The tensile damage at the arch springing of the conventional composite structure is distributed in an upward convex shape along the longitudinal direction of the tunnel; specifically, the damage value in the range of the fault fracture zone is quite large, and the damage value in the range of the hanging wall and footwall is small. After adopting the new composite structure, the damage presents a downward convex distribution, which differs from that of the conventional composite structure. Compared with that of conventional concrete, the damage tolerance of the ECC is significantly larger; when the traditional concrete material is replaced with high-toughness ECC in the fault area, the damage of the structure decreases under the same seismic intensity, and the damage tolerance of the structure and aseismic performance are significantly improved.

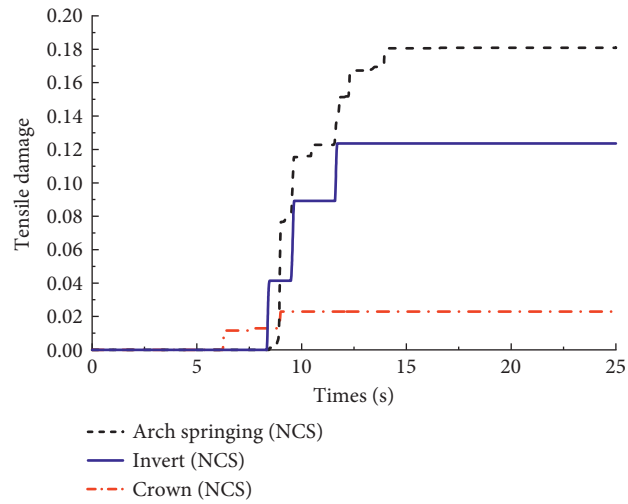

Figure 11: Damage time history curve of typical point of the lining section.

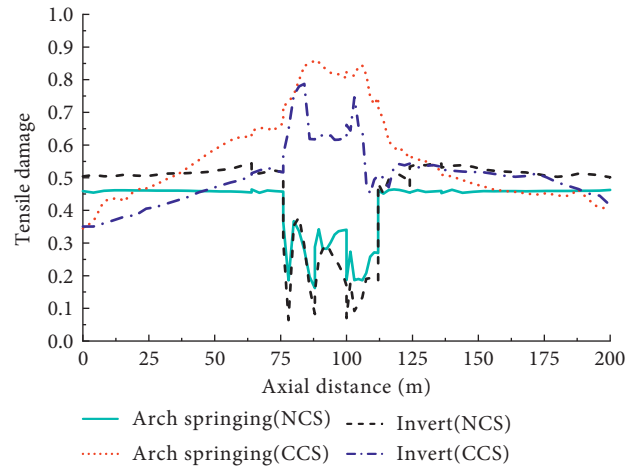

Figure 12: Damage distribution along the tunnel.

5.1.4. Displacement Response. Figure 13 shows the lateral displacement distribution curves of typical parts of the composite lining structure at the moment of peak acceleration. The lateral displacement distribution laws of different parts of the lining are similar, and the structural displacement in the fault fracture zone area shows remarkable changes. The maximum dislocation displacement is approximately 1.5 cm. This type of misalignment is mainly concentrated in the range of 85–110 m in the longitudinal direction of the model, and the order of displacement changes is arch springing > invert > crown > spandrel > sidewall.

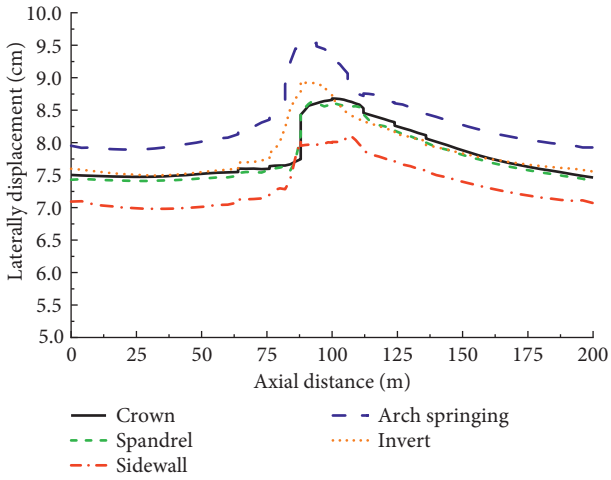

Figure 13: Distribution curve of the laterally displacement of typical parts of the lining along the axial.

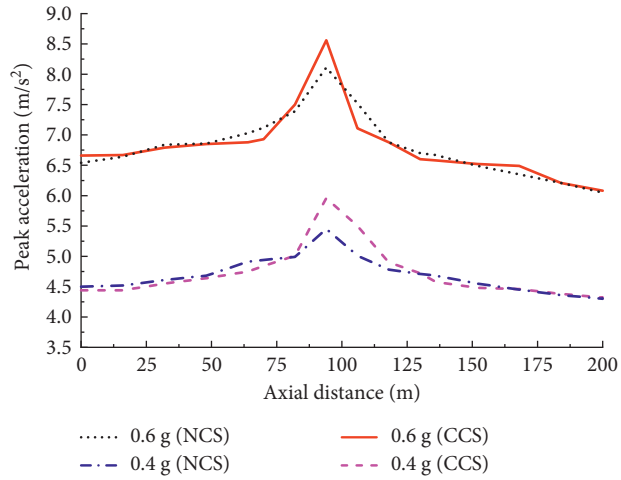

Figure 14: Changes in the peak acceleration of the composite structure along the axial of the tunnel.

5.2. Effects of Seismic Intensity. Changes in the distribution curve of the peak acceleration at the arch springing of the composite structure along the tunnel under the seismic intensity of 0.4 and 0.6 g are shown in Figure 14.

Figure 14 demonstrates that the peak acceleration response distribution laws of the two combined structures are similar under different seismic intensities, and a certain acceleration amplification response could be observed in the area of the fault fracture zone. At seismic intensity of 0.4 g, compared with those of the hanging wall and footwall regions, the acceleration magnifications of the new and conventional composite structures in the fault area are 1.08 and 1.16, respectively. When the seismic intensity increases to 0.6 g, the acceleration magnifications of the new and conventional composite structures in the fault area are 1.11 and 1.18, respectively. As the intensity of seismic increases, the acceleration response of the structure in the fault area also increases, which is mainly manifested as an increase in acceleration magnification. However, under the same seismic intensity, the acceleration response of the two types of composite structures differs; compared with the conventional composite structure, the new composite lining structure can effectively reduce the acceleration amplification response, and the reduction range is between 5.90% and 6.90%.

At the seismic intensity of 0.6 g, the damage distribution of the two types of composite structures, as shown in Figure 15. Combining Figures 10 and 15, the peak seismic acceleration could be observed to increase from 0.4 g to 0.6 g; such acceleration significantly increases the severity and distribution of damage in various parts of the tunnel structure. For example, the damaged area at the arch springing of the lining increases by over twofold. Under the same seismic intensity, the new composite structure only suffers local damage at the invert and arch springing in the fault fracture zone. The conventional composite structure shows full-circle closed tension and compression damage, and the damage range is larger than that of the new composite structure. Moreover, the spandrels and sidewalls of the new composite structure are only slightly damaged when the seismic acceleration peak is 0.6 g. By contrast, the conventional composite structure lining is seriously damaged at 0.4 g. These results demonstrate that the new composite structure has good aseismic applicability.

Figure 16 shows that the overall lateral displacement of the tunnel structure and displacement of the fault zone increases as the intensity of seismic increases. When the peak seismic acceleration increases from 0.4 g to 0.6 g, the maximum displacement increases from 1.5 cm to 2.5 cm, which is an increase of approximately 66.7%. Compared with that of the conventional composite structure, the response displacement value of the new composite structure is slightly smaller, but the displacement response law is generally the same.

5.3. Effects of Seismic Direction. The damage of the linings of the two composite lining structures under the action of axial seismic waves (peak acceleration, 0.4 g) is shown in Figure 17. Figures 17 and 10 reveal that, under the action of axial seismic waves, the overall damage of the tunnel structure increases because of the axial tension and compression of the longitudinal seismic; hence, the damage area of the structure and damage degree in the fault fracture zone increase. The direction of seismic activity clearly influences the seismic response of the composite structure, and the aseismic effect of the composite structure is closely related to the direction of the seismic waves. Thus, research on seismic resistance in tunnel must consider the influence of seismic direction.

Regardless of the direction of seismic activity, the damage of the conventional composite structures in the area of the fault fracture zone is serious, and the distribution range of this damage penetrates the entire lining section. By comparison, the damage distribution range and damage concentration area of the new composite structure are significantly reduced. Under the action of

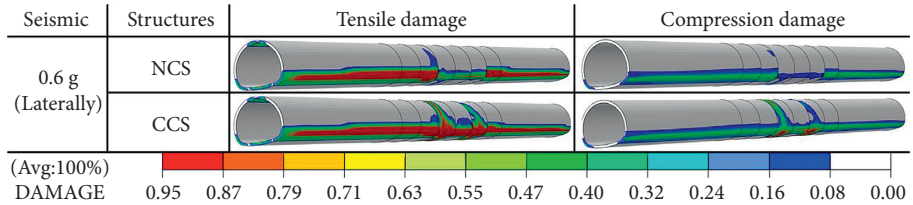

Figure 15: Lining damage distribution.

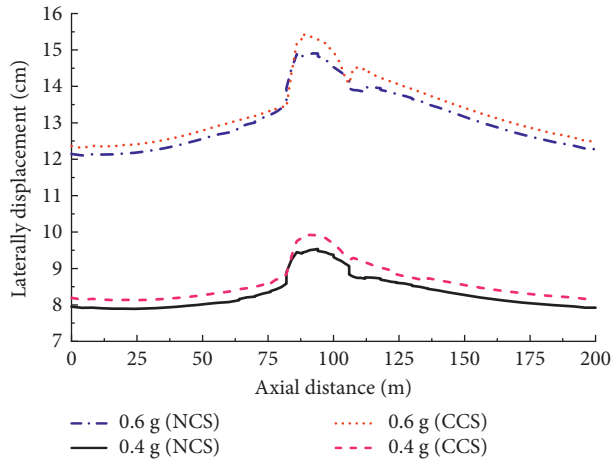

Figure 16: Laterally displacement of the footwall under different seismic intensities.

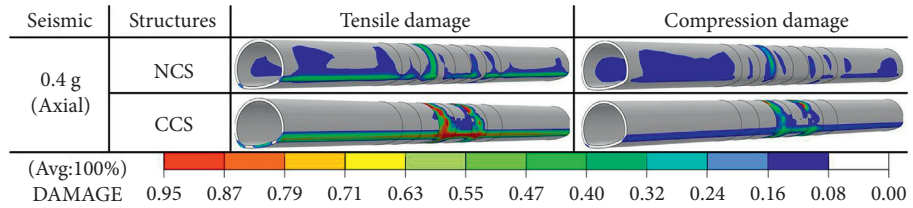

Figure 17: Cloud diagrams of the lining damage distribution under the axial seismic.

seismic waves in two different directions, the new composite structure shows better aseismic performance and applicability to earthquake directions.

6. Conclusions

(1) According to the uniaxial tensile and compression test results, the peak tensile stress and tensile strain of the ECC are approximately 1.3 and 327.0 times those of C30 ordinary concrete; the respective peak compressive stress and corresponding strain of the former are also approximately 1.4 and 3.0 times those of the latter. These findings reveal that the ECC has excellent tensile and compressive toughness and could effectively compensate for the shortcomings of ordinary concrete, which include fragility and easy cracking.

(2) ECC materials are used to replace conventional concrete in the fault fracture zone and construct a new composite structure. The seismic response characteristics of the new composite structure are similar to those of the conventional composite structure. The structures in the fault fracture zone and adjacent areas demonstrate obvious acceleration amplification responses, and the stress and displacement responses are also larger. Compared with that of the conventional aseismic composite structure, the damage tolerance of the new composite lining structure is significantly improved. The damage degree and distribution area are significantly reduced, and the acceleration amplification and displacement responses in the fault area are effectively reduced. Thus, the new composite structure has better aseismic effects than the conventional structure.

(3) Under different seismic intensities, the damage and displacement responses of the new composite structure in the area of the fault fracture zone are smaller than those of the conventional composite structure. When the peak acceleration is increased from 0.4 g to 0.6 g, the damage degree and distribution area of each part of the two composite structures are significantly increased and the displacement of the fault zone is obvious. Compared with the conventional composite structure,

the new composite structure has better aseismic effects and adaptability to seismic activity of different intensities.

(4) Regardless of the direction of seismic action (i.e., laterally or axial), the damage distribution of the conventional composite structure in the area of the fault fracture zone is more serious than that of the new composite structure. Thus, the latter has better seismic resistance and applicability to the seismic directions. Compared with laterally seismic activity, the damage range of the two composite structures is significantly increased under axial seismic activity. The applicability of the new composite structure to seismic activity in the lateral direction is better than that to the axial.

Data Availability

The data used to support the findings of this study are included within the article.

Conflicts of Interest

The authors declare that they have no conflicts of interest.

Acknowledgments

This research was supported by the National Natural Science Foundation of China (Grant no. 52168057) and Science and Technology Project of Yunnan Provincial Department of Transportation (Grant no. 2017A-04).

References

[1] G. Y. Cui, M. N. Wang, L. Yu, and G. Lin, "Study on the characteristics and mechanism of seismic damage for tunnel structures on fault rupture zone in Wenchuan seismic disastrous area," *China Civil Engineering Journal*, vol. 46, no. 11, pp. 122–127, 2013.

[2] Y. S. Shen, Z. Z. Wang, J. Yu, X. Zhanga, and B. Gao, "Shaking table test on flexible joints of mountain tunnels passing through normal fault," *Tunnelling and Underground Space Technology incorporating Trenchless Technology Research*, vol. 98, Article ID 103299, 2020.

[3] Y. S. Chen, *Earthquake Damage Investigation of Wenchuan Earthquake Highway-Geological Disaster*, People's Communications Press, Beijing, China, 2012.

[4] L. Li, C. He, and P. Geng, "Analysis of seismic dynamic responses of tunnel through fault zone in high earthquake intensity area," *Journal of Chongqing University*, vol. 35, no. 6, pp. 92–98, 2012.

[5] C. He, L. Li, J. Zhang, and P. Geng, "Seismic damage mechanism of tunnels through fault zones," *Chinese Journal of Geotechnical Engineering*, vol. 36, no. 3, pp. 427–434, 2014.

[6] Y. Liu, J. Lai, J. P. Xin, X. D. Li, and R. J. Xing, "Comparison test of dynamic response characteristics of the tunnels through fault," *Rock and Soil Mechanics*, vol. 40, no. 12, pp. 4693–4702, 2019.

[7] P. Geng, J. L. Tang, Q. L. Quan, and C. He, "Shaking table test for tunnel with shock absorption layer though fault zone," *Journal of Central South University*, vol. 44, no. 6, pp. 2520–2526, 2013.

[8] M. N. Wang and G. Y. Cui, "Study of the mechanism of shock absorption layer in the supporting system of tunnels in highly seismic areas," *China Civil Engineering Journal*, vol. 44, no. 8, pp. 126–131, 2011.

[9] Z. Z. Jin, *Study on Seismic Response of Damping Structure of Tunnel through Fault Zone*, Southwest Jiaotong University, Sichuan, China, 2014.

[10] M. D. Lepech and V. C. Li, "Water permeability of engineered cementitious composites," *Cement and Concrete Composites*, vol. 10, no. 31, pp. 744–753, 2009.

[11] D.-Y. Yoo, J. Kim, G. Zi, and Y.-S. Yoon, "Effect of shrinkage-reducing admixture on biaxial flexural behavior of ultra-high-performance fiber-reinforced concrete," *Construction and Building Materials*, vol. 89, pp. 67–75, 2015.

[12] J. Zhang, C. Gong, and Z. Guo, "Engineered cementitious composite with characteristic of low drying shrinkage," *Cement and Concrete Research*, vol. 4, no. 39, pp. 303–312, 2009.

[13] S. L. Xu, N. Wang, and X. H. Cai, "Experimental study of post-pouring UHTCC simply supported two-way concrete slab under concentrated load," *China Civil Engineering Journal*, vol. 44, no. 8, pp. 33–41, 2011.

[14] Gb/T50081-2016, *Standard for Test Methods of Ordinary concrete Mechanical Properties*, China Construction Industry Press, Beijing, China, 2016.

[15] J. Lee and G. L. Fenves, "Plastic-damage model for cyclic loading of concrete structures," *Journal of Engineering Mechanics*, vol. 124, no. 8, pp. 892–900, 1998.

[16] J. Lubliner, J. Oliver, S. Oller, and E. Oñate, "A plastic-damage model for concrete," *International Journal of Concrete Structures and Materials*, vol. 25, no. 3, pp. 299–326, 1989.

[17] D. Meng, C. K. Lee, and Y. X. Zhang, "Flexural and shear behaviours of plain and reinforced polyvinyl alcohol-engineered cementitious composite beams," *Engineering Structures*, vol. 151, pp. 261–272, 2017.

[18] X. Li, X. Zhou, Y. Tian, and M. Li, "A modified cyclic constitutive model for engineered cementitious composites," *Engineering Structures*, vol. 179, pp. 398–411, 2019.

[19] M. Cao, "Research on damage plastic calculation method of ABAQUS concrect damage plasticity model," *Transportation Research*, no. 2, pp. 51–54, 2012.

[20] J. Yu, J. Yao, X. Lin et al., "Tensile performance of sustainable Strain-Hardening Cementitious Composites with hybrid PVA and recycled PET fibers," *Cement and Concrete Research*, vol. 107, pp. 110–123, 2018.

[21] L. Li, Z. Cai, K. Yu, Y. X. Zhang, and Y. Ding, "Performance-based design of all-grade strain hardening cementitious composites with compressive strengths from 40 MPa to 120 MPa," *Cement and Concrete Composites*, vol. 97, pp. 202–217, 2019.

[22] J. Yu, Y. Chen, and C. K. Y. Leung, "Mechanical performance of Strain-Hardening Cementitious Composites (SHCC) with hybrid polyvinyl alcohol and steel fibers," *Composite Structures*, vol. 226, Article ID 111198, 2019.

[23] J. Yu, J. Lin, Z. Zhang, and V. C. Li, "Mechanical performance of ECC with high-volume fly ash after sub-elevated temperatures," *Construction and Building Materials*, vol. 99, pp. 82–89, 2015.

[24] Z. Zhang, Q. Zhang, S. Qian, and V. C. Li, "Low E modulus early strength engineered cementitious composites material," *Transportation Research Record: Journal of the Transportation Research Board*, vol. 2481, no. 1, pp. 41–47, 2015.

[25] L. Xu, C. Wei, and B. Li, "Damage evolution of steel-polypropylene hybrid fiber reinforced concrete: experimental and

numerical investigation," *Advances in Materials Science and Engineering*, vol. 2018, Article ID 1719427, 23 pages, 2018.

[26] M. I. Khan and G. Fares, "Effect of temperature on strain capacity and cracking system of SHCC of different workability and SAP contents," *Construction and Building Materials*, vol. 213, pp. 337–347, 2019.

[27] K. Yu, L. Li, J. Yu, Y. Wang, J. Ye, and Q. Xu, "Direct tensile properties of engineered cementitious composites: a review," *Construction and Building Materials*, vol. 165, pp. 346–362, 2018.

[28] Q. J. Chen, X. Q. Li, and G. T. Liu, "Study on the properties of ECC and its finite element application," *China Concrete and Cement Products*, no. 12, pp. 50–53, 2017.

[29] X. Li, X. Yang, Z. Ding, X. Du, and J. Wen, "ECC design based on uniform design test method and alternating conditional expectation," *Mathematical Problems in Engineering*, vol. 2019, Article ID 9575897, 14 pages, 2019.

[30] X. Q. Li, X. Yang, and Z. D. Ding, "Optimized mix proportion design of ECC based on the UDEM-ACE method," *Materials Reports*, vol. 33, no. 7, pp. 2354–2361, 2019.

[31] Z. D. Ding, J. C. Wen, X. Q. Li, and X. Yang, "Impermeability and splitting tensile test of PVA-ECC and existing concrete bonding interface," *Journal of Building Materials*, vol. 22, no. 3, pp. 356–362, 2019.

[32] The Professional Standards Compilation Group of People's Republic of China, *GB50010—2010 Code for Design of concrete Structures*China Architecture and Building Press, Beijing, China, 2010.

[33] Q. F. Shan, J. L. Pan, and J. H. Chan, "Mechanical behaviors of steel reinforced ECC/concrete composite columns under combined vertical and horizontal loading," *Journal of southeast University*, vol. 31, no. 2, pp. 259–265, 2015.

[34] W. Q. Zhang, *Study on the Seismic Damage Mechanism of Tunnels through Fault and Anti-seismic and Damping*, Southwest Jiaotong University, Sichuan, China, 2012.

[35] G. Y. Cui, M. N. Wang, and L. Yu, "Model test research on damping Technology of damping joints in fractured sticky-slip tunnel," *Chinese Journal of Rock Mechanics and Engineering*, vol. 32, no. 8, pp. 1603–1609, 2013.

[36] H. Xu and T. B. Li, "Seismic dynamic response and damping effect analysis of different buffer layers on tunnels," *China Civil Engineering Journal*, vol. 44, no. S1, pp. 201–208, 2011.

[37] G. Y. Cui, L. Ji, and H. F. Jing, "Damping shake Technology of the shock absorption layer of fault-crossing tunnels in a dangerous mountainous area with high-intensity earthquakes," *China Earthquake Engineering Journal*, vol. 41, no. 2, pp. 286–291, 2019.

[38] J. D. Byerlee and J. C. Savage, "Coulomb plasticity within the fault zone," *Geophysical Research Letters*, vol. 19, no. 23, pp. 2341–2344, 1992.

[39] Z. L. Wang, C. R. He, and Y. S. Zhou, "Stress state and frictional strength obtained with frictional experiments of fault," *Chinese Journal of Rock Mechanics and Engineering*, vol. 23, no. 23, pp. 4079–4083, 2004.

[40] F. Wang, Z. Q. Song, Y. J. Liu, and C. Su, "Research on static-dynamic unified artificial boundary based on ABAQUS infinite element," *Journal of Water Resources and Water Engineering*, vol. 2018, Article ID 7828267, 14 pages, 2018.

[41] K. H. Twana, F. Asaad, M. Nicole, D. Chapman, and F. Rahimzadeh, "Development of an infinite element boundary to model gravity for subsurface civil engineering applications," *International Journal for Numerical and Analytical Methods in Geomechanics*, vol. 44, no. 3, pp. 418–431, 2020.